Alignment Does Matter: Design Thick Electrodes to Improve the Comprehensive Lithium Storage Performance

Bo Nie[a], Mingxin Li[b], Tiankai Yao[b], Haoqing Yang[a], Linrui Duan[a], Juchen Zhang[a], Guoqing Xin[b], Tengxiao Liu[c], Hongtao Sun[a,d*], Jie Lian[b*]

[a]*The Harold & Inge Marcus Department of Industrial & Manufacturing Engineering,* [c]*Department of Biomedical Engineering,* [d]*Materials Research Institute (MRI), The Pennsylvania State University, University Park 16802, Pennsylvania, USA*

[b]*Department of Mechanical Aerospace and Nuclear Engineering, Rensselaer Polytechnic Institute, New York 12180, USA*

ABSTRACT

Developing electrochemical energy storage that enables simultaneously delivering high areal, volumetric, and gravimetric performance is a grand fundamental and technological challenge. It is straightforward but problematic to make electrodes thicker and denser for high areal and volumetric performance while sustaining a high level of gravimetric performance. The insufficient charge transports in these electrodes with high mass loading and electrode density could severely degrade the energy storage performance. Herein, we developed an energy-efficient fast sintering method (*e.g.*, Spark Plasma Sintering) to fabricate a structural cathode with a high electrode density (2.0-2.3 g cm^{-3}) and high mass loading (70-100 mg cm^{-2}). The vertically aligned carbon networks and anisotropic pore channels in the ultrathick electrodes (300-500 μm) are designed and tailored for efficient charge transports throughout the whole thickness. As a result, the sintered structural electrodes perform high areal (8.6 mAh cm^{-2}), volumetric

* Corresponding authors.

Tel: 518-276-6081. E-mail: lianj@rpi.edu (Jie Lian)

Tel: 814-865-1489. E-mail: hzs5373@psu.edu (Hongtao Sun)

capacity (246 mAh cm^{-3}), uncompromised gravimetric performance (164 mAh g^{-1}) at normal current (<2 mA cm^{-2}), and stable cycling with a capacity retention of 84% after 200 cycles under a current density of 4.5 mA cm^{-2}.

Keywords: alignment, thick electrode, fast sintering, lithium-ion batteries

1. Introduction

There is a growing technological demand for high-performance electrochemical energy storage (EES), which can meet the requirements of expanding markets for portable electronics, electrification of transportation, and grid storage [1-4]. Traditional EES devices usually consist of anode and cathode thin films sandwiched between two current collector foils and isolated by insulator separators [5,6]. This stacking sequence is repeated to achieve desirable energy and power outputs. There is considerable interest in creating EES devices that are smaller and lighter while delivering high levels of energy and power. Thus, it is straightforward to improve the overall performance of a battery device by increasing the electrode density and areal mass loadings of electroactive materials [7, 8, 9, 10]. However, in most cases, the previously developed electrodes can only possess high performance based on one metric but perform poorly on other metrics [11-15]. For instance, high gravimetric performance is usually achieved at low areal mass loadings (mg cm^{-2}) or/and low electrode density (g cm^{-3}), leading to low areal or/and volumetric performance. Complementary metrics (e.g., gravimetric, areal, and volumetric) are equally essential to evaluate real EES devices for practical applications. To the best of our knowledge, very few electrodes reported today have high storage performance in all three-performance metrics. Only some of the best electrodes can perform well on more than one metric [4,7,8,16,17].

Nanostructured electrodes with tailored porosity have shown great promise because of their short charge transport pathways and high charge delivery rates [3, 11, 13, 18]. However, high performance is only obtained in electrodes with relatively low areal mass loadings and low electrode density, which cannot readily be translated to

practical battery devices [12, 18, 19]. As a result, the promise of these nanostructured electrodes shows little practical relevance. For example, sustaining the same specific capacity and current density in thicker electrodes requires proportionally higher charge delivery rates [4]. The inevitable trade-off between high electrode density (for fast electron transport) and high porosity (for rapid ion transport) cannot result in simultaneously high volumetric and gravimetric storage performance [20-22]. All of these suggest that the high performance of practical devices that requires thicker and denser electrodes is primarily constrained by the increasing charge transport limitations [4,23]. Hence, delivering high areal and volumetric storage performance with sustaining high gravimetric performance represents a fundamental scientific challenge.

Here we fabricate a structural electrode consisting of a vertically aligned carbon network (graphene-CNTs) using a fast spark plasma sintering (SPS) process. Under this heat and densification process, the various electrode building blocks (*e.g.*, carbon-coated $LiFePO_4$: C-LFP, graphene sheets, CNTs) can be fast assembled and integrated into a bulk form. While the carbon networks are well aligned with a preferential orientation perpendicular to the uniaxial pressure applied [5,24]. The sintered bulk pellet can be sectioned into thick electrodes (300-500 μm) with vertically aligned carbons (e.g., C-LFP-100-V and C-LFP-50-V electrodes). The highly interconnected carbon network in the thick electrode can provide excellent electron transport properties, especially along the in-plane direction of the aligned graphene nanosheets. At the same time, high-pressure sintering creates anisotropic pore structures perpendicular to the pressure applied [5] and along the same direction as aligned carbon networks. Therefore, the thick electrodes with vertically aligned carbons and pore channels (*e.g.*, C-LFP-100-V and C-LFP-50-V electrodes) for fast electron and ion transports can deliver better lithium storage performance than the sectioned thick electrodes with laterally aligned charge transport pathways (*e.g.,* C-LFP-100-L and C-LFP-50-L electrodes). Impressively, the dense and thick electrode (2.0-2.3 g cm^{-3}, 70-100 mg cm^{-2}) with vertically aligned charge transport pathways performs high areal (8.6 mAh cm^{-2}) and volumetric (246 mAh cm^{-3}) energy storage, as well as the uncompromised gravimetric performance (164 mAh g^{-1}) at normal current (<2 mA cm^{-2}). More importantly, only

one thick cathode needs to be paired with an anode in a new battery configuration for high energy output. This can replace the current battery configuration of repeatedly stacking thin-film anodes and cathodes. The new configuration using thick electrodes lowers the weight and cost of inactive carrying materials and simplifies the battery assembly process.

2. Material and Methods

2.1. Materials. The commercial carbon-coated $LiFePO_4$ (C-LFP) powders were purchased from Jiangsu Fangzhou New Energy Co., Ltd. Multi-wall carbon nanotubes (CNTs) were purchased from Nanostructured & Amorphous Materials Inc. Graphene sheets were obtained by thermal exfoliation and reduction of the graphite oxide (GO) prepared from graphite powder following the Hummers method.

2.2. Fabrication of Thick Electrodes. The C-LFP powders were first well-mixed with graphene sheets and CNTs by HEBM, and this mixture as the initial compound (~75 wt% C-LFP, 25 wt% graphene-CNT additives) was then consolidated/assembled into a bulk pellet by a fast SPS process under uniaxial pressure of 10 MPa applied on the graphite die outside. The bulk pellets were sintered under various heating rates (*e.g.*, 100 and 50 ℃ min^{-1}) until reaching the desired temperature of 400 ℃ and directly cooling down to room temperature. The bulk pellets are not robust if the heating rate is higher than 100 ℃ min^{-1}; pellets are too dense for ion transport if the heating rate is lower than 50 ℃ min^{-1}. The sectioned thick electrodes with vertical and lateral alignments of conductive carbon additives were obtained by vertically and horizontally cutting from the sintered bulk pellet using the diamond saw at a cutting speed of 700 rpm, respectively. The cutting thickness was controlled by the micrometer integrated with the diamond saw. The thick electrodes with vertically aligned carbons are designated as C-LFP-100-V/C-LFP-50-V (vertical section facing up), and ones with laterally aligned carbons are designated as C-LFP-100-L/C-LFP-50-L (lateral section facing up). Because the original sintered bulk pellets are cylindrical shape, the vertically and the laterally sectioned electrodes result in rectangular and circular shapes,

respectively.

2.3. Material Characterizations. The morphological and structural characteristics were conducted by scanning electron microscopy (SEM, Zeiss Supra 40VP), transmission electron microscopy (TEM, JEOL), X-ray diffraction (XRD) (Panalytical X'Pert Pro X-ray Powder Diffractometer). Thermogravimetric analysis (TGA, PerkinElmer instruments Pyris Diamond TG/DTA) was conducted in an air atmosphere from room temperature to 750 °C at a heating rate of 10 °C min^{-1}.

2.4. Alignment Measurements by Polarized Raman Spectroscopy. Polarized Raman spectroscopy experiments were conducted using a Raman microscope (Raman-11, Nanophoton Corp.). The excitation laser beam, with a wavelength of 532 nm, was polarized after passing through a polarizer and focused onto a sample through an objective lens (100x, NA 0.9). The polarization direction was controlled with a half-wave plate between the objective lens and the polarizer. The polarized Raman intensity depends on the polarization angle, θ, of the laser beam, and the angular dependence of the Raman peak intensity, I(θ), is fitted with the following equation:

$$I(x) = \left(\frac{6}{7}\cos^2\theta - \frac{2}{7}\right)\langle \mathrm{P}_2(\cos\theta)\rangle + \left(\cos^4\theta - \frac{6}{7}\cos^2\theta + \frac{3}{35}\right)\langle \mathrm{P}_4(\cos\theta)\rangle + \frac{1}{5} \quad (1)$$

where $<P_2(\cos\theta)>$ and $<P_4(\cos\theta)>$ are the second-and forth-order orientation parameters, respectively. $<P_2(\cos\theta)>$ is known as the nematic order parameter, S, equal to 1 for a perfect alignment and 0 for a complete random orientation.

2.5. Preparation of Slurry Electrodes. The slurry-coated electrodes as a control were prepared by mixing 80 wt % active materials (C-LFP), 10 wt % acetylene black (super-Li), and 10 wt % polyvinylidene fluoride (PVDF) binder dissolved in N-methyl-2-pyrrolidinone (NMP). After coating on Al foils, electrodes were dried at 80 ℃ under vacuum for 16 h to remove the solvent and then punched into a disk and pressed. The mass loading of the electrode material is around 1.5 mg cm^{-2}.

2.6. Electrochemical Measurements. All the electrodes were assembled into CR 2032

coin cells with a lithium foil as the counter electrode, Celgard 2340 membrane separator, and 1 M LiPF6 electrolyte solution dissolved in a 1: 1 (v/v) mixture of ethylene carbonate (EC) and dimethyl carbonate (DMC). The cells were assembled in an argon-filled glove box with moisture and oxygen contents below 1.0 ppm. Galvanostatic charge-discharge cycles were tested in a voltage window of 2.5-4.2 V using an Arbin Instrument at various rates of 0.1-1.0 C. CV was performed at a scan rate of 0.1 mV s^{-1} using Versa STAT 4 electrochemical workstation (Ametek, Princeton Applied Research). Electrochemical impedance spectroscopy measurements were performed at open circuit potential with a sinusoidal signal in a frequency range from 100 kHz to 10 mHz at an amplitude of 10 mV. Two identical electrodes were assembled into a symmetric cell to determine ionic resistance for EIS measurements of non-faradaic processes. Additionally, the half-cell EIS characterizations and the corresponding equivalent circuit simulation were conducted to obtain the kinetic parameters. Galvanostatic intermittent titration technique (GITT) test was conducted to determine the Li^+ diffusion kinetics of the assembled cell for all the thick electrodes. Specifically, the assembled cells were applied with t = 30 min GITT pulse current at 0.1 C rate. After each titration step, the cells were allowed to relax for 4 hours. This procedure was repeated until the cut-off potentials (2.7 V and 4.2 V).

3. Results and Discussion

3.1. Fabrication of Thick Electrodes

The thick electrodes were prepared by mechanical mixing and rapid high-temperature sintering (Fig. 1). Briefly, the 50-150 nm carbon-coated $LiFePO_4$ (C-LFP) (Fig. 1a and Fig. S1) and conductive graphene-CNT additives (see weight percentages in Fig. S2) were first well-mixed by high energy ball milling (HEBM) (Fig. 1b, and Fig. S3 (a)). This mixture was then densified/assembled into a bulk pellet by a fast SPS process under 10 MPa uniaxial pressure applied on the graphite dies wrapped outside

(Fig. 1c). The benefit of this SPS process is the mitigation of particle/crystal growth and generation of strong bonding between compounds in the sintered body by varying three major process parameters (i.e., pressure, temperature, and high-density current) [25,26]. During this rapid compacting and sintering process, as-consolidated bulk pellets can easily possess high pellet density and mitigate the crystal grain growth of active electrode materials.

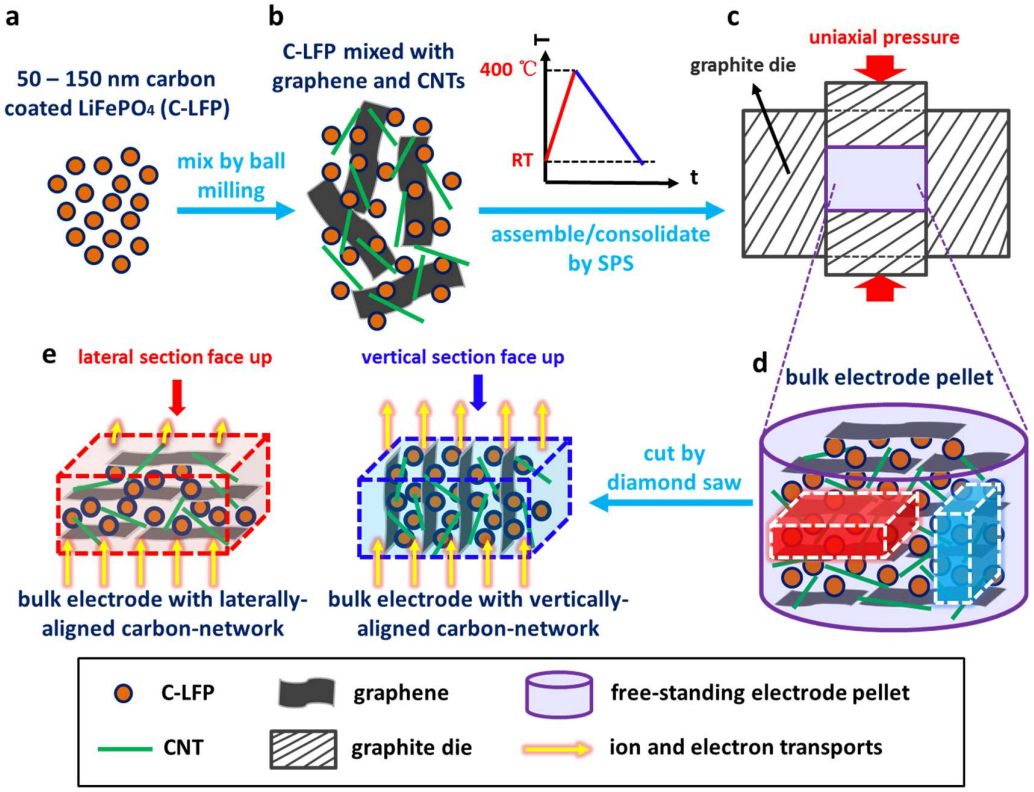

Fig. 1. Illustration of the process flow to fabricate thick electrodes with aligned charge transport pathways. (**a**) 50-150 nm carbon-coated $LiFePO_4$ (C-LFP). (**b**) C-LFP nanoparticles uniformly mixed with graphene sheets and CNTs by HEBM. (**c**) Free-standing C-LFP bulk pellets assembled/consolidated by fast SPS under uniaxial pressure. (**d**) The bulk pellet with preferentially aligned carbon network perpendicular to the uniaxial pressure applied during the sintering process. (**e**) Sectioned thick electrodes with the vertical or lateral alignment of the carbon networks. The yellow arrows indicate the favorable charge transport pathways for ions and electrons.

More interestingly, the conductive graphene-CNT networks and anisotropic pore channels are orthogonal to the uniaxial pressure applied upon SPS fabrication (Fig.

1d) [5,27]. The gradually aligned 2D graphene components during the SPS sintering results from the shear force induced sliding along the graphene layers due to the weak intermolecular force (e.g., van der Waals force). Thus, the deflection of graphene layers causes the flow and plastic deformation of the $LiFePO_4$ powders under the uniaxial pressure. The deflection of multi-layered graphene sheets continues sliding until the shear force along the layers turns zero when graphene-CNT networks are completely perpendicular to the pressure direction [28]. The as-prepared bulk pellet was cut horizontally and vertically to obtain thick electrodes with laterally and vertically aligned carbon networks, respectively (Fig. 1e). Due to the preferential direction of electron and ion transports along aligned conductive carbons and pore channels [5,29], the thick electrode with vertically aligned charge transport pathways can deliver charges more efficiently than the electrode with laterally aligned transport pathways.

3.2. Characterizations of Microstructures and Alignments

Here two bulk pellets with different porosities (see details in the Supplementary Information) were fabricated to demonstrate their morphological, structural, and electrochemical properties (Figs. S3-S5). The bulk pellets are identified as C-LFP-100 and C-LFP-50 for SPS processes with 100 ℃ min^{-1} and 50 ℃ min^{-1} heating rates, respectively. By controlling the heating rate, pore structures can be tailored for optimization of ionic transport, in which greater porosity (33% vs. 25%) was achieved for the bulk pellet with a fast-heating rate. The various sizes of dies were used to control the dimension of the free-standing bulk pellets (*e.g.*, a diameter of 8.0-15.0 mm and a height of 6.0-8.0 mm), as shown in Fig. 2a and Fig. S4. The plain view SEM images of the laterally sectioned bulk pellet (Fig. 2b and c) display the micron-sized composite flakes with sintering-induced necking (Fig. 2b). The particle size in C-LFP-100 pellet sintered at a relatively high heating rate (100 ℃ min^{-1}) is constrained to around 100-150 nm after SPS process (Fig. 2c). While the cross-sectional SEM images of the vertically sectioned pellet (Fig. 2d and e) show a dramatically distinct morphology with a relatively rough surface and pores as a result of an aligned graphene-CNT network

that is orthogonal to the uniaxial pressure applied [27]. The alignment of the conductive carbon network and anisotropic pore structure may facilitate electron and ion transports along their preferential directions [30,31]. The C-LFP-50 pellet sintered at a relatively low heating rate (50 °C min^{-1}) shows a slightly different morphology (Fig. S3 b-e) compared to the C-LFP-100 pellet. The graphene sheets and CNTs are uniformly distributed around the $LiFePO_4$ particles, which is confirmed by the elementary mapping (Fig. S3 f-j). Both C-LFP-100-L and C-LFP-50-L pellets show densely compacted materials with a few random pores and gaps at some localized regions. Additionally, the X-ray diffraction (XRD) studies of C-LFP compounds before and after the SPS process show unchanged XRD peaks (Fig. 2f), indicating the maintained structure and crystal size during this rapid sintering process. The orientation order of the carbon network in these thick electrodes is further verified by using polarized Raman spectroscopy.

In principle, Raman scattering is only allowed for an in-plane polarization of the incident and scattered lights but is prohibited in the perpendicular polarization direction [27,32,33]. As shown in our Raman measurement setup (Fig. 2g), the in-plane direction of the thick fractured electrodes is in the x-y plane while the polarization is changing in the x-z plane. A series of Raman spectra are taken at different polarization angles (θ) (Fig. 2h), and all the D-band (1346 cm^{-1}), G-band (1577 cm^{-1}), and 2D-band (2680 cm^{-1}) peaks noticeably vary in Raman intensity with polarization angles. The angular dependence of the G-band intensity is polar-plotted and fitted with Equation 1 (see Fig. 2i). Therein, the G-band intensity becomes most considerable as the polarization of the light is parallel to the in-plane axis of the thick electrodes (i.e., θ = 0 and 180°) and becomes smallest as the polarization is normal to the x-y plane (i.e., θ = 90 and 270°). In addition, based on Equation 1, the nematic order parameter S [33-35], which represents the strength of alignment, is calculated to be 0.60 and 0.53 (1 for perfect alignment and 0 for complete random orientation) for C-LFP-100-V and C-LFP-50-V thick electrodes respectively. By all the characterization above, the conductive graphene-CNT additives are strongly aligned inside bulk pellets and sectioned

electrodes.

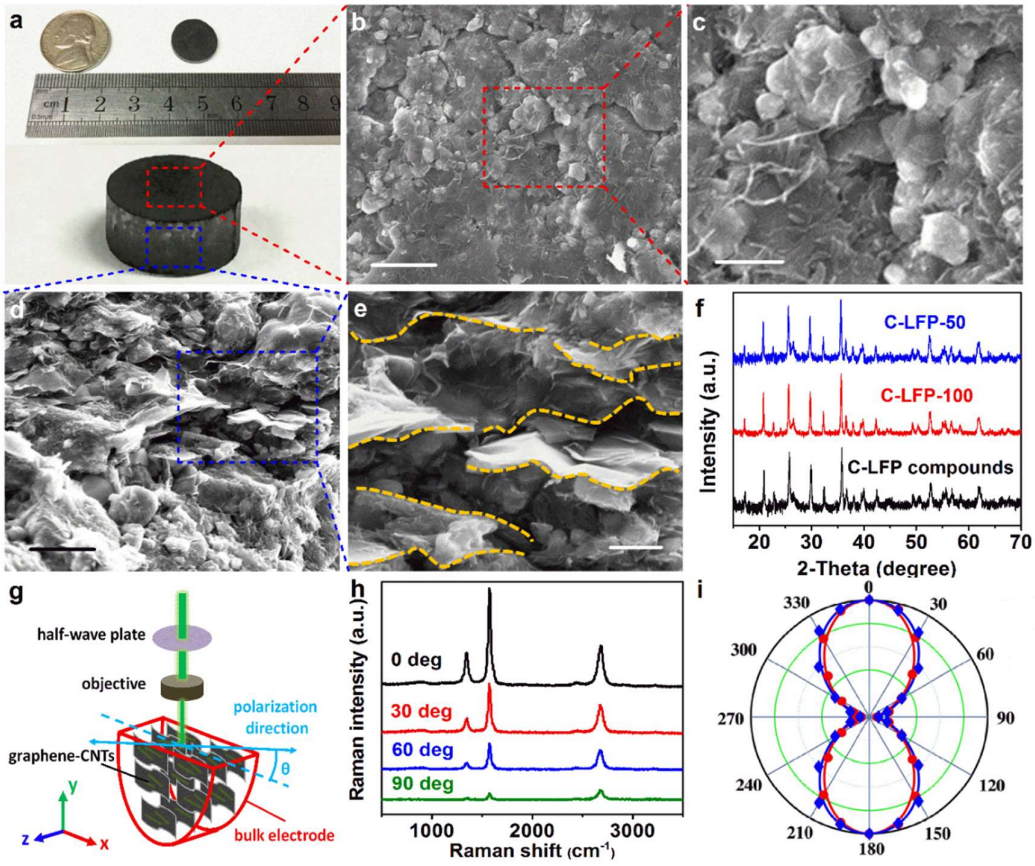

Fig. 2. Microstructure and alignment characterizations of free-standing C-LFP thick electrodes. (**a**) A digital camera image of an as-fabricated C-LFP-100 bulk pellet. (**b,c**) SEM images of a lateral-sectional view of the bulk pellet. (**d,e**) SEM images of a vertical-sectional view of the bulk pellet. (**f**) XRD spectra of C-LFP compounds before and after the rapid sintering process at different heating rates (50 and 100 °C min^{-1}). (g) Measurement setup for polarized Raman spectroscopy. (**h**) Raman spectra taken at different polarization angles, θ = 0, 30, 60, 90 deg. (**i**) A polar diagram showing the normalized intensity of the G-band as a function of θ. The red circle and solid line represent the experimental data and fitting curve of the C-LFP-100-V thick electrode; the blue diamond and solid line represent the experimental data and fitting curve of the C-LFP-50-V thick electrode. Scale bars, 1.0 μm (b,d,), 200 nm (c,e,).

3.3. Alignment-Enabled Control of Electrochemical Properties

By the aligned conductive carbon network and corresponding anisotropic

porosity, the preferential pathways for both electrons and ions play an essential role in the charge transport kinetics and electrochemical properties of the thick electrodes. To probe the charge transport kinetics, we conducted electrochemical impedance spectroscopy (EIS) measurements on thick electrodes (300-500 μm) by using a symmetric cell with two identical electrodes. Before lithiation, the Nyquist plots of a symmetric cell describe a non-faradaic process with a state of charge (SOC) at 0 %. The projection of the 45-degree slope, as indicated by bold lines to the real axis, reflects the ionic resistance ($R_{ion}/3$) of the electrolyte-filled pores inside the thick electrodes (Fig. 3a and Fig. S5), which is the limiting factor for sufficient charge transports in a thick and dense electrode during the charge/discharge process [4,36,37]. The C-LFP-100-V thick electrode with a higher porosity of 33% (Fig. S5a) shows lower ionic resistance as indicated by a shorter projection length than the C-LFP-50-V thick electrode with a relatively lower porosity of 23% (Fig. S5c) because of its more efficient electrolyte-filled pathways for ion transports. At the same porosity, compared with the C-LFP-100-L thick electrode with laterally aligned carbon network and pore channels (Fig. S5b), the decrease in ionic resistance for the C-LFP-100-V electrode with vertically aligned carbon networks and anisotropic pores (Fig. S5a) indicates that the ion transport kinetics can be improved by optimizing the orientation of fast ion transport pathways. The denser C-LFP-50-L electrode with lateral alignments (Fig. S5d) shows a large semicircle with another curved tail because it is difficult for ions to travel through such a dense and thick electrode. The high resistance of the semicircle could result from a considerable interface resistance between the liquid electrolyte and solid thick electrodes. Meanwhile, the impedance analysis of the assembled half-cells has been carried out with the equivalent circuit simulation to get the corresponding kinetic parameters for four thick electrodes (*e.g.*, R_{sol}, R_{ct}, and Warburg diffusion coefficient) (Fig. S6 and Table S1). Specifically, the *Rct* and Warburg diffusion resistance follow decreasing trends from the C-LFP-50-L, C-LFP-50-V, C-LFP-100-L, and C-LFP-100-V. Based on the EIS results and fitting parameters, the electrodes with vertically aligned carbon networks and associated porosity exhibit better charge transfer and diffusion kinetics.

In addition, cyclic voltammetry (CV), charge-discharge, and dQ/dV tests were carried out to compare different structured electrodes (Fig. 3b). Due to a relatively lower electrode density, C-LFP-100-L and C-LFP-100-V electrodes sintered at 100 ℃ min^{-1} showed a smaller separation between anodic and cathodic redox peaks than the C-LFP-50-L, and C-LFP-50-V electrodes sintered at the 50 ℃ min^{-1} in the CV curves, which indicates a reduced polarization due to an improved mass transfer between an anode and a cathode. Their corresponding charge/discharge curves follow similar variations among different electrodes (Fig. 3 c, d). All the electrodes show a typical $LiFePO_4$ charge-discharge behavior with different polarizations. The separations between charge and discharge curves are increasing in the order of C-LFP-100-V, C-LFP-100-L, C-LFP-50-V, and C-LFP-50-L, indicating decreased mass transfer kinetics. Because of the large thickness (~300-500 μm) and relatively high electrode density (2.0 g cm^3 -2.3 g cm^{-3}), the C-LFP-100-V electrode illustrates an increasing capacity offset as increasing the current densities from 0.1 C to 1C due to the polarization (Fig. 3e). The variation of polarization between the charge and discharge plateaus is further analyzed by the dQ/dV curves (Fig.S7). To confirm the diffusion kinetics, we employed the galvanostatic intermittent titration technique (GITT) to characterize the Li^+ diffusion coefficients for four different thick electrodes (Fig. S8). The C-LFP-100-V thick electrode with vertically aligned conductive network presents much higher Li^+ diffusion coefficients (~10^{-14} cm^2 s^{-1} vs. ~10^{-16} cm^2 s^{-1}) compared to the C-LFP-100-L with laterally aligned charge transport pathways, which indicates a favorable charge transport pathways across the thickness direction inside the electrode.

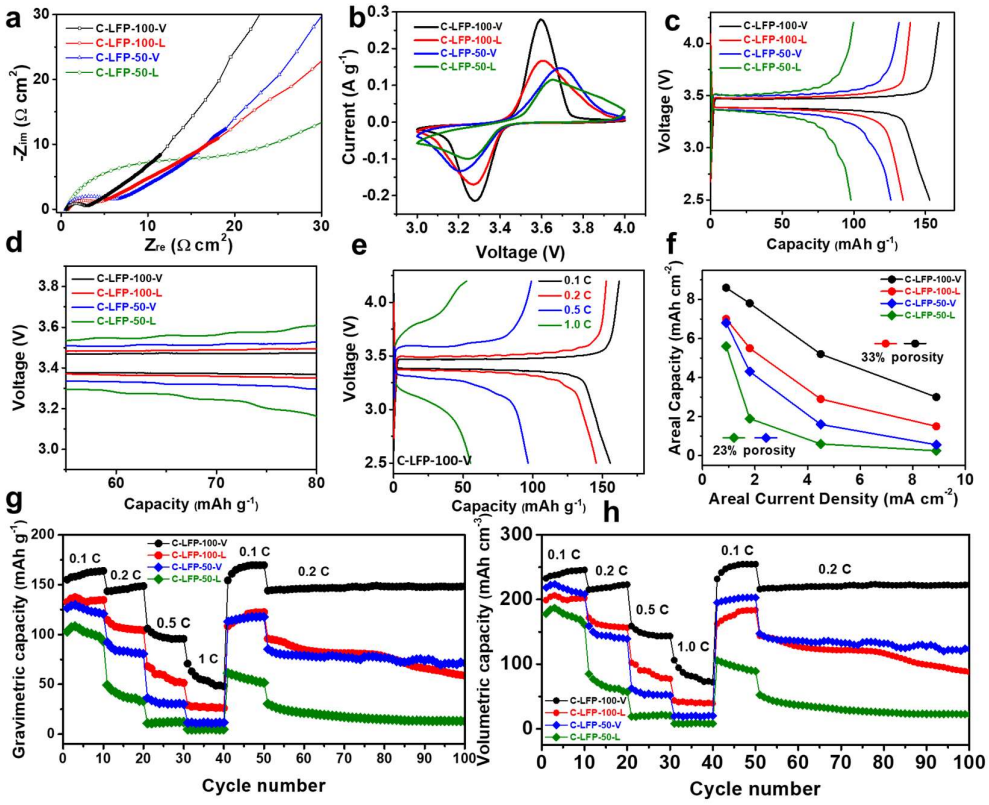

Fig. 3. Effects of alignment on comprehensive electrochemical characteristics. (**a**) The Nyquist plots were compared from potentiostatic EIS of a symmetric cell using two identical electrodes (~100 mg cm^{-2}) at a state of charge (SOC) 0%. The projection of the slope in the high-frequency region is used to determine the ionic resistance for the electrolyte-filled porous architectures in a non-faradaic process. (**b**) The cyclic voltammetry of the assembled half-cells for various thick electrodes at a scan rate of 0.1 mV s^{-1}. (**c, d**) The charge-discharge curves of the half-cells at 0.1 C. A zoom-in charge-discharge curves for the comparison in (d). (**e**) The charge-discharge curves of C-LFP-100-V electrode at various C-rate of 0.1-1.0 C. (**f**) Areal capacity as a function of areal current density. The comparison of gravimetric capacity (**g**) and volumetric capacity (**h**) at various C-rates for thick electrodes with different orientations of aligned carbons and various porosities. The thicknesses of thick electrodes are around 300-500 μm. The laterally sectioned electrodes have a diameter of 8 mm, and vertically sectioned electrodes have a side length of 7.7-8.4 mm (area: 60 – 70 mm^2).

We carried out galvanostatic studies to examine the rate performance of these thick electrodes. As demonstrated in Fig. 3f-h and Fig. S9, the thick electrodes with a higher porosity (*e.g.*, 33% for C-LFP-100 electrodes) consistently exhibit higher capacity in three aspects of metrics (gravimetric, areal, and volumetric performance) for a given current compared to the thick electrodes with a lower porosity (*e.g.*, 23% for C-LFP-50 electrodes). This is because of the increasing charge transport limit of ions in electrolyte-filled pores as the electrodes become denser, severely degrading the storage capacity [2,4,5,38]. More interestingly, the thick electrodes with vertically aligned carbons and pore channels (C-LFP-100-V, C-LFP-50-V) possess noticeably higher performance in all three aspects of metrics than the laterally aligned electrodes (C-LFP-100-L, C-LFP-50-L). The anisotropic pores lead to low-tortuosity pore channels, which provide sufficient charge transport along its preferential orientation through the whole thick electrodes [5,38,39]. As a result, the C-LFP-100-V thick electrode can deliver an areal capacity of around 8.6 mAh cm^{-2} at the current density of ~ 1 mA cm^{-2}, which is more than three times as much capacity as slurry-coated LFP electrodes (2.5 mAh cm^{-2}, table S2). At a high current of ~9 mA cm^{-2}, it can still output a practical level of areal capacity of ~3 mAh cm^{-2}. Moreover, our optimized C-LFP-100-V thick electrodes can perform higher volumetric capacity (245 mAh cm^{-3}) compared to other counterpart thick electrodes (*e.g.*, C-LFP-100-L, C-LFP-50-V, C-LFP-50-L electrodes) due to its optimized charge transports (Fig. 3h).

3.4. Assessment of the Storage Performance in Three Aspects of Metrics

Addressing the fundamental challenges of increasing diffusion limitations in thick and dense electrodes can improve electrochemical performance. For instance, our C-LFP-100-V thick electrode (70 mg cm^{-2}) with optimized vertical charge transport pathways can deliver stable cycling performance with high-capacity retention of over 84 % and high Coulombic efficiency of around 99.6 % over 200 cycles at the current of 4.5 mA cm^{-2} (Fig. 4a). The cycled thick electrode was opened and further characterized by SEM after washing with acetonitrile, ethanol, and water to remove the

residual electrolyte. As shown in Fig. S10, the cycled electrode can maintain the alignments after prolonged charge-discharge cycles.

Furthermore, the advantage of having high mass loadings of active materials in electrodes becomes more apparent when inactive components (*e.g.*, carbons, binders, and current collectors) are considered to calculate the capacity based on the total weight of the electrode [1,4]. As demonstrated in Fig. 4b, the specific capacity normalized by the active material mass (164 mAh g^{-1}) for our thick electrode with a mass loading of 70 mg cm^{-2} will be reduced by 31% (from 164 to 113 mAh g^{-1}) when the capacity is normalized by the total mass of electrode materials and current collectors (6 mg cm^{-2}); while for an electrode with a low mass loading of 1.9 mg cm^{-2} [40], the corresponding translated specific capacity (per weight of the electrode and current collector) is reduced by >80% (from 154 to 30 mAh g^{-1}). Thus, even with a high-performance material, when the mass loading is low, the performance of the active materials has much less influence on the device performance because the weight of the electrochemically inactive components (*e.g.*, current collector) dominates the total electrode weight [1,4]. The inclusion of cell packaging will further diminish the performance of practical devices. More importantly, the high mass-loaded thick electrode can be integrated into a new configuration of the battery cell that employs only one pair of a thick anode and a thick cathode instead of repeatedly stacking of thin-film anode//separator//cathode to meet the demanding energy and power outputs (Fig. S11). This new configuration enables us to save the weight and cost of inactive carrying materials (*e.g.*, separators, current collectors, and packing) and simplify the battery cell assembly process.

The inevitable trade-off between high gravimetric performance (high porosity) and high volumetric performance (high electrode density) prevents many high-performance electrodes in the lab scale from being used in practical applications where the volume is at a premium [1]. In this work, the volumetric performance of our thick electrodes (246 mAh cm^{-3}) is superior to other nano-sized and micro-sized $LiFePO_4$ cathodes (Fig. 4c) because of its high electrode density and optimized charge transport pathways [40-43]. Moreover, our thick electrodes with vertically optimized charge

transport pathways for both ions and electrons can deliver better performance in all three aspects of performance metrics (i.e., gravimetric, volumetric, and areal performance) than other electrodes reported previously (Fig. 4d and Table S2).

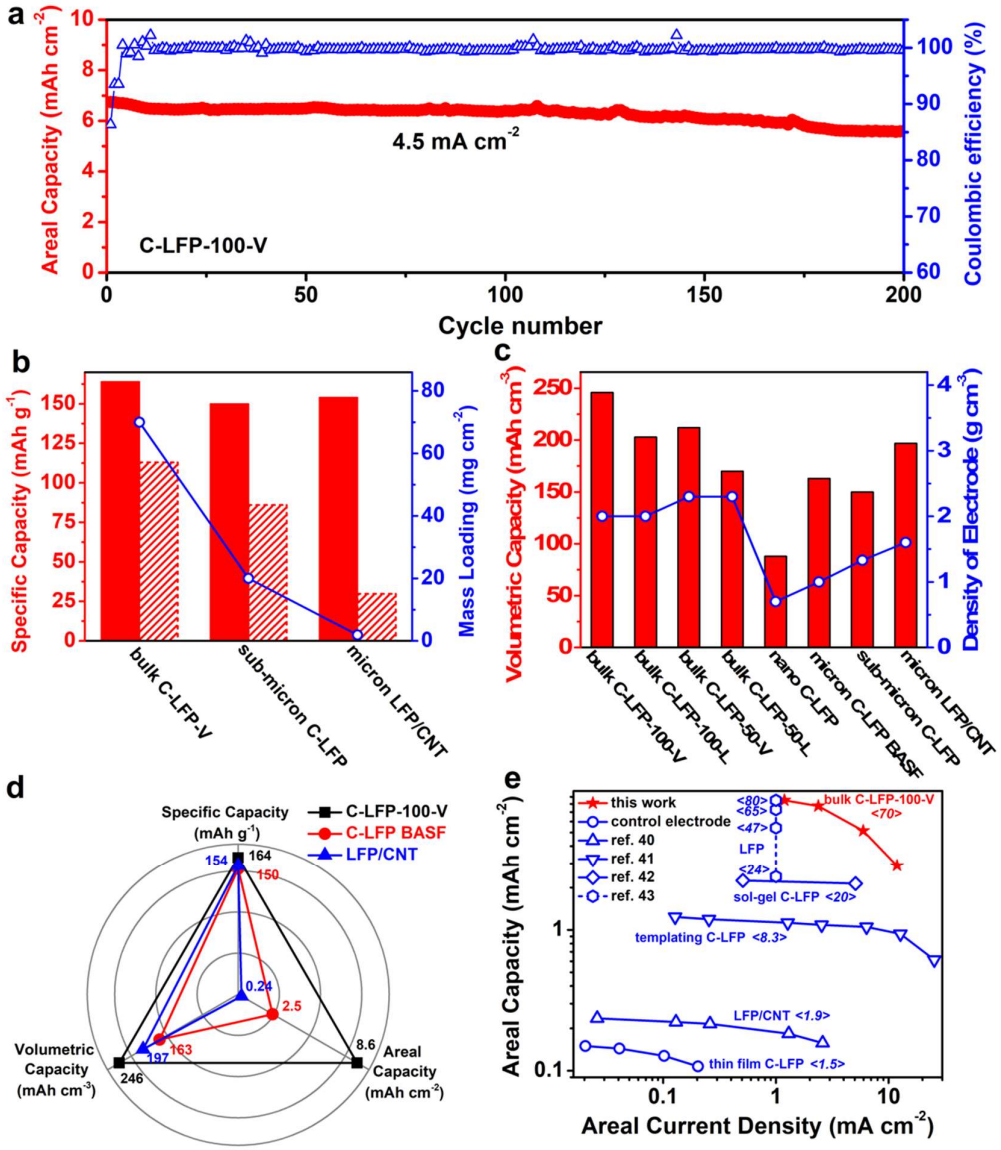

Fig. 4. Comprehensive battery performance for thick electrodes. (a) The long cycling performance of the C-LFP-100-V thick electrode (70 mg cm^{-2}) measured at a current density of 4.5 mA cm^{-2}. (**b**) The comparison of specific capacity (at 0.1C) normalized by the active $LiFePO_4$ materials (solid bars) with specific capacity normalized by the total weight of active materials, carbons, binders, and metal current collector (~6 mg cm^{-2}) (shaded bars) for our bulk electrodes and other representative

$LiFePO_4$ cathodes with different mass loading (blue line). (**c**) The comparison of volumetric capacity of our optimized thick electrodes with thick counterpart electrodes and various representative $LiFePO_4$ cathodes at 0.1C. (**d**) The comprehensive comparison among three performance metrics. (**e**) The comparison of areal performance metrics of the C-LFP-100-V thick electrode with other $LiFePO_4$ cathodes reported previously. The numbers in the angle brackets indicate the areal mass loadings of the electrode materials.

We also compare the areal capacity vs. current density with representative $LiFePO_4$ cathodes (Fig. 4e) [40-43]. In contrast to other cathodes, our thick electrode at a high mass loading of 70 mg cm^{-2} exhibits more than three times as much areal capacity as previous cathodes at a practical mass loading of 20 mg cm^{-2} (*e.g.*, sol-gel C-LFP) and more than 40 times as much as that of lab-scale thin-film cathodes (*e.g.*, control electrode: thin-film C-LFP) at a low mass loading of 1.5 mg cm^{-2}.

4. Conclusion

In summary, we demonstrated the importance of aligning the conductive carbon networks and pore channels to achieve high-performance energy storage at simultaneous high mass loadings and electrode density. The C-LFP-100-V thick electrode with vertically aligned conductive carbons and anisotropic pore channels exhibits more efficient ion and electron transports due to their favorable charge transport pathways. The optimized thick electrode can deliver an enhanced areal capacity of 8.6 mAh cm^{-2} and a volumetric capacity of 246 mAh cm^{-3} with sustained gravimetric performance at a current density of 0.1C. Achieving high performance in all three respects of metrics represents an essential step toward practical EES devices. Moreover, our optimized thick electrode enables stable cycling with a capacity retention of 84% after 200 cycles under a current density of 4.5 mA cm^{-2}. In the future, sacrificial pore-formers can be involved to further improve the ion transport rate for high-power performance; high ionic conductors can also be integrated inside bulk pellets for all-solid-state batteries. (ASSBs).

Declaration of Competing interests

The authors declare no competing financial interests.

CrediT authorship contribution statement

Bo Nie: Conceptualization, Methodology, Formal analysis, Investigation, Writing – original draft, Visualization, Writing – review & editing. **Mingxin Li**: Methodology, Validation, Investigation. **Tiankai Yao**: Validation, Investigation. **Haoqing Yang**: Methodology, Investigation, Validation. **Linrui Duan**: Validation, Visualization, Writing – review & editing. **Juchen Zhang**: Methodology, Visualization, Writing – review & editing. **Guoqing Xin**: Validation, Investigation. **Tengxiao Liu**: Methodology, Writing – review & editing. **Hongtao Sun**: Conceptualization, Methodology, Investigation, Writing – original draft, Writing – review & editing, Supervision, Funding acquisition. **Jie Lian**: Writing – original draft, Writing – review & editing, Supervision, Funding acquisition.

Acknowledgements

JL acknowledges financial support from National Science Foundation award (2119423). HS would like to thank National Science Foundation FMSG (2134643) and Pennsylvania State University start-up fund for partial support of this work.

Appendix. Supporting materials

Supplementary information is available in the online version of the paper.

References

[1] Y. Gogotsi and P. Simon, True Performance Metrics in Electrochemical Energy Storage, Science 334 (2011) 917-918, doi: 10.1126/science.1213003

[2] K. G. Gallagher, S. E. Trask, C. Bauer, T. Woehrle, S. F. Lux, M. Tschech, P. Lamp, B. J. Polzin, S. Ha, B. Long, Q. L. Wu, W. Q. Lu, D. W. Dees and A. N. Jansen, Optimizing Areal Capacities through Understanding the Limitations of Lithium-Ion Electrodes, J. Electrochem. Soc. 163 (2016) A138-A149, doi: 10.1149/2.0321602jes

[3] J. Wu, X. Zhang, Z. Ju, L. Wang, Z. Hui, K. Mayilvahanan, K. J. Takeuchi, A. C. Marschilok, A. C. West, E. S. Takeuchi and G. Yu, From Fundamental Understanding to Engineering Design of High-Performance Thick Electrodes for Scalable Energy-Storage Systems, Adv. Mater. 33 (2021) 2101275-2101291, doi: https://doi.org/10.1002/adma.202101275

[4] H. T. Sun, L. Mei, J. F. Liang, Z. P. Zhao, C. Lee, H. L. Fei, M. N. Ding, J. Lau, M. F. Li, C. Wang, X. Xu, G. L. Hao, B. Papandrea, I. Shakir, B. Dunn, Y. Huang and X. F. Duan, Three-dimensional holey-graphene/niobia composite architectures for ultrahigh-rate energy storage, Science 356 (2017) 599-604, doi: 10.1126/science.aam5852

[5] J. S. Sander, R. M. Erb, L. Li, A. Gurijala and Y. M. Chiang, High-performance battery electrodes via magnetic templating, Nat. Energy 1 (2016) 16099-16106, doi: 10.1038/nenergy.2016.99

[6] M. Armand and J. M. Tarascon, Building better batteries, Nature 451 (2008) 652-657, doi: 10.1038/451652a

[7] Z. Y. Ju, Y. Zhu, X. Zhang, D. M. Lutz, Z. W. Fang, K. J. Takeuchi, E. S. Takeuchi, A. Marschilok and G. H. Yu, Understanding Thickness-Dependent Transport Kinetics in Nanosheet-Based Battery Electrodes, Chem. Mater. 32 (2020) 1684-1692, doi: 10.1021/acs.chemmater.9b05396

[8] Z. Han, S. Li, R. Xiong, Z. Jiang, M. Sun, W. Hu, L. Peng, R. He, H. Zhou, C. Yu, S. Cheng and J. Xie, Low Tortuosity and Reinforced Concrete Type Ultra-Thick Electrode for Practical Lithium–Sulfur Batteries, Adv. Funct. Mater. 32 (2022) 2108669, doi: https://doi.org/10.1002/adfm.202108669

[9] S. Li, G. Tian, R. Xiong, R. He, S. Chen, H. Zhou, Y. Wu, Z. Han, C. Yu, S. Cheng and J. Xie, Enhanced homogeneity of electrochemical reaction via low tortuosity enabling high-voltage nickel-rich layered oxide thick-electrode, Energy Storage Mater. 46 (2022) 443-451, doi: https://doi.org/10.1016/j.ensm.2022.01.035

[10] R. He, G. Tian, S. Li, Z. Han, W. Zhong, S. Cheng and J. Xie, Enhancing the Reversibility of Lithium Cobalt Oxide Phase Transition in Thick Electrode via Low Tortuosity Design, Nano Lett. 22 (2022) 2429-2436, doi: 10.1021/acs.nanolett.2c00123

[11] Z. G. Liu, J. L. Zhu, D. Z. Lu, W. Wang, L. G. Yue and Y. Y. Li, Fabricating ultrathick, dense electrodes for compact rechargeable batteries with ultrahigh areal and volumetric capacity, J. Power Sources 523 (2022) 231046-231056, doi: 10.1016/j.jpowsour.2022.231046

[12] S. P. Li, R. Y. Xiong, Z. L. Han, R. J. He, S. W. Li, H. M. Zhou, C. Yu, S. J. Cheng and J. Xie, Unveiling low-tortuous effect on electrochemical performance toward ultrathick LiFePO4 electrode with 100 mg cm(-2) area loading, J. Power Sources 515 (2021) 230588- 230597, doi: 10.1016/j.jpowsour.2021.230588

[13] K. Yang, L. Y. Yang, Z. J. Wang, B. Guo, Z. B. Song, Y. Fu, Y. C. Ji, M. Q. Liu, W. G. Zhao, X. H. Liu, S. C. Yang and F. Pan, Constructing a Highly Efficient Aligned Conductive Network to Facilitate Depolarized High-Areal-Capacity Electrodes in Li-Ion Batteries, Adv. Energy Mater. 11 (2021) 2100601-2100609, doi: 10.1002/aenm.202100601

[14] Y. L. Zhao, J. G. Feng, X. Liu, F. C. Wang, L. F. Wang, C. W. Shi, L. Huang, X.

Feng, X. Y. Chen, L. Xu, M. Y. Yan, Q. J. Zhang, X. D. Bai, H. A. Wu and L. Q. Mai, Self-adaptive strain-relaxation optimization for high-energy lithium storage material through crumpling of graphene, Nat. Commun. 5 (2014) 5565-5573, doi: 10.1038/ncomms5565

[15] J. Zhu, Y. Shan, T. Wang, H. T. Sun, Z. P. Zhao, L. Mei, Z. Fan, Z. Xu, I. Shakir, Y. Huang, B. G. Lu and X. F. Duan, A hyperaccumulation pathway to three-dimensional hierarchical porous nanocomposites for highly robust high-power electrodes, Nat. Commun. 7 (2016) 13432-13442 doi: 10.1038/ncomms13432

[16] J. Park, C. Jeon, W. Kim, S. J. Bong, S. Jeong and H. J. Kim, Challenges, laser processing and electrochemical characteristics on application of ultra-thick electrode for high-energy lithium-ion battery, J. Power Sources 482 (2021) 228948-228957 doi: 10.1016/j.jpowsour.2020.228948

[17] Y. X. Xu, Z. Y. Lin, X. Zhong, X. Q. Huang, N. O. Weiss, Y. Huang and X. F. Duan, Holey graphene frameworks for highly efficient capacitive energy storage, Nat. Commun. 5 (2014) doi: 10.1038/ncomms5554

[18] H. T. Sun, G. Q. Xin, T. Hu, M. P. Yu, D. L. Shao, X. Sun and J. Lian, High-rate lithiation-induced reactivation of mesoporous hollow spheres for long-lived lithium-ion batteries, Nat. Commun. 5 (2014) 4526-4534, doi: 10.1038/ncomms5526

[19] H. T. Sun, X. Sun, T. Hu, M. P. Yu, F. Y. Lu and J. Lian, Graphene-Wrapped Mesoporous Cobalt Oxide Hollow Spheres Anode for High-Rate and Long-Life Lithium Ion Batteries, J. Phy. Chem. C 118 (2014) 2263-2272, doi: 10.1021/jp408021m

[20] G. Li, T. Ouyang, T. Xiong, Z. Jiang, D. Adekoya, Y. Wu, Y. Huang and M. S. Balogun, All-carbon-frameworks enabled thick electrode with exceptional high-areal-capacity for Li-Ion storage, Carbon 174 (2021) 1-9, doi: https://doi.org/10.1016/j.carbon.2020.12.018

[21] L. Liu, G. Li, T. Ouyang, S. A. Ogundare, X. Yao and M. S. Balogun, 3D carbon networks/NiO nanosheets thick electrodes for high areal capacity lithium ion batteries, Electrochem. Commun. 139 (2022) 107306, doi: https://doi.org/10.1016/j.elecom.2022.107306

[22] Y. Wu, T. Ouyang, T. Xiong, Z. Jiang, Y. Hu, J. Deng, Z. Wang, Y. Huang and M.-S. Balogun, Boosted Storage Kinetics in Thick Hierarchical Micro–Nano Carbon Architectures for High Areal Capacity Li-Ion Batteries, Energy & Environ. Mater. 5 (2022) 1251-1259, doi: https://doi.org/10.1002/eem2.12241

[23] H. M. Cheng and F. Li, Charge delivery goes the distance, Science 356 (2017) 582-583, doi: 10.1126/science.aan1472

[24] A. Boden, B. Boerner, P. Kusch, I. Firkowska and S. Reich, Nanoplatelet Size to Control the Alignment and Thermal Conductivity in Copper-Graphite Composites, Nano Lett. 14 (2014) 3640-3644, doi: 10.1021/nl501411g

[25] R. Elango, A. Nadeina, F. Cadiou, V. De Andrade, A. Demortiere, M. Morcrette and V. Seznec, Impact of electrode porosity architecture on electrochemical performances of 1 mm-thick LiFePO4 binder-free Li-ion electrodes fabricated by Spark Plasma Sintering, J. Power Sources 488 (2021) 229402-229411, doi: 10.1016/j.jpowsour.2020.229402

[26] E. Dumont-Botto, C. Bourbon, S. Patoux, P. Rozier and M. Dolle, Synthesis by Spark Plasma Sintering A new way to obtain electrode materials for lithium ion batteries, J. Power Sources 196 (2011) 2274-2278, doi: 10.1016/j.jpowsour.2010.09.037

[27] W. Ji, H. Qu, X. Zhang, D. Zheng and D. Qu, Electrode Architecture Design to Promote Charge-Transport Kinetics in High-Loading and High-Energy Lithium-Based Batteries, Small Methods 5 (2021) 2100518-2100540, doi: https://doi.org/10.1002/smtd.202100518

[28] C. Sun, Y. Huang, n. Qiang Shen, W. Wang, W. Pan, P. a. Zong, L. Yang, Y. Xing and C. Wan, Embedding two-dimensional graphene array in ceramic matrix, Sci. Adv. 6 eabb1338, doi: 10.1126/sciadv.abb1338.

[29] Z. Y. Nie, R. Parai, C. Cai, C. Michaelis, J. M. LaManna, D. S. Hussey, D. L. Jacobson, D. Ghosh and G. M. Koenig, Pore Microstructure Impacts on Lithium Ion Transport and Rate Capability of Thick Sintered Electrodes, J. Electrochem. Soc. 168 (2021) doi: 10.1149/1945-7111/ac0bf6

[30] H. Yang, T. Xiong, Z. Zhu, R. Xiao, X. Yao, Y. Huang and M. S. Balogun, Deciphering the lithium storage chemistry in flexible carbon fiber-based self-supportive electrodes, Carbon Energy 4 (2022) 820-832, doi: 10.1002/cey2.173

[31] Y. Wu, T. Ouyang, H. Yang, F. Wang and M. S. Balogun, Engineering graphite microfiber-based thick electrodes as anode material for lithium ion batteries, Inorganic Chem. Commun. 128 (2021) 108611, doi: https://doi.org/10.1016/j.inoche.2021.108611

[32] T. Liu and S. Kumar, Quantitative characterization of SWNT orientation by polarized Raman spectroscopy, Chem. Phy. Lett. 378 (2003) 257-262, doi: 10.1016/s0009-2614(03)01287-9

[33] S. Ushiba, S. Shoji, K. Masui, J. Kono and S. Kawata, Direct Laser Writing of 3D Architectures of Aligned Carbon Nanotubes, Adv. Mater. 26 (2014) 5653-+, doi: 10.1002/adma.201400783

[34] S. Ushiba, S. Shoji, K. Masui, P. Kuray, J. Kono and S. Kawata, 3D microfabrication of single-wall carbon nanotube/polymer composites by two-photon polymerization lithography, Carbon 59 (2013) 283-288, doi: 10.1016/j.carbon.2013.03.020

[35] J. Shaver, A. N. G. Parra-Vasquez, S. Hansel, O. Portugall, C. H. Mielke, M. von Ortenberg, R. H. Hauge, M. Pasquali and J. Kono, Alignment Dynamics of Single-

Walled Carbon Nanotubes in Pulsed Ultrahigh Magnetic Fields, Acs Nano 3 (2009) 131-138, doi: 10.1021/nn800519n

[36] N. Ogihara, S. Kawauchi, C. Okuda, Y. Itou, Y. Takeuchi and Y. Ukyo, Theoretical and Experimental Analysis of Porous Electrodes for Lithium-Ion Batteries by Electrochemical Impedance Spectroscopy Using a Symmetric Cell, J. Electrochem. Soc. 159 (2012) A1034-A1039, doi: 10.1149/2.057207jes

[37] N. Ogihara, Y. Itou, T. Sasaki and Y. Takeuchi, Impedance Spectroscopy Characterization of Porous Electrodes under Different Electrode Thickness Using a Symmetric Cell for High-Performance Lithium-Ion Batteries, J. Phy. Chem. C 119 (2015) 4612-4619, doi: 10.1021/jp512564f

[38] X. S. Wu, S. X. Xia, Y. Q. Huang, X. C. Hu, B. Yuan, S. J. Chen, Y. Yu and W. Liu, High-Performance, Low-Cost, and Dense-Structure Electrodes with High Mass Loading for Lithium-Ion Batteries, Adv. Funct. Mater. 29 (2019) doi: 10.1002/adfm.201903961

[39] T. Q. Wu, Z. D. Zhao, J. J. Zhang, C. Zhang, Y. X. Guo, Y. J. Cao, S. X. Pan, Y. C. Liu, P. Y. Liu, Y. H. Ge, W. Liu, L. Dong and H. B. Lu, Thick electrode with thickness-independent capacity enabled by assembled two-dimensional porous nanosheets, Energy Storage Mater. 36 (2021) 265-271, doi: 10.1016/j.ensm.2020.12.034

[40] M. Chen, C. Y. Du, B. Song, K. Xiong, G. P. Yin, P. J. Zuo and X. Q. Cheng, High-performance LiFePO4 cathode material from FePO4 microspheres with carbon nanotube networks embedded for lithium ion batteries, J. Power Sources 223 (2013) 100-106, doi: 10.1016/j.jpowsour.2012.09.040

[41] D. P. Singh, F. M. Mulder, A. M. Abdelkader and M. Wagemaker, Facile Micro Templating LiFePO4 Electrodes for High Performance Li-Ion Batteries, Adv. Energy Mater. 3 (2013) 572-578, doi: 10.1002/aenm.201200704

[42] J. S. Yang and J. J. Xu, Synthesis and characterization of carbon-coated lithium transition metal phosphates LiMPO4 (M = Fe, Mn, Co, Ni) prepared via a nonaqueous sol-gel route, J. Electrochem. Soc. 153 (2006) A716-A723, doi: 10.1149/1.2168410

[43] S. F. Yang, Y. N. Song, K. Ngala, P. Y. Zavalij and M. S. Whittingham, Performance of LiFePO4 as lithium battery cathode and comparison with manganese and vanadium oxides, J. Power Sources 119 (2003) 239-246, doi: 10.1016/s0378-7753(03)00240-4